X-ray Nano Computed Tomography of Electrospun Fibrous Mats as Flow Battery Electrodes

Rhodri Jervis[1], Matt D. R. Kok[2], Julian Montagut[2], Jeff T. Gostick[3], Dan J. L. Brett[1], Paul R. Shearing[1]

[1]Electrochemical Innovation Lab, Department of Chemical Engineering, University College London, UK

[2]Department of Chemical Engineering, McGill University, Montreal, Canada

[3]Porous Media Engineering and Analysis Lab, Department of Chemical Engineering, University of Waterloo, Canada

Abstract

Many electrochemical energy storage and conversion devices employ porous media as electrodes, gas diffusion layers or separators. Recently, electrospinning has received significant attention as a way to generate nano-fibers of polymers with controlled morphology and properties that, once carbonised, can act as conductive and porous media for electrochemical energy devices. The recent advances in X-ray computed tomography have led the technique to

be widely used in the characterisation of energy technologies and porous media as it offers a uniquely non-destructive insight into the 3D microstructure of materials. Here we present electrospun fibrous mats with uncontrolled, controlled and aligned morphology for use as redox flow battery electrodes and, for the first time, obtain ultra-high resolution nano-tomographic X-ray imaging of the materials using a lab source. The virtual 3D volumes enable extraction of parameters that would not be possible via other characterisation routes.

1. Introduction

Redox flow batteries (RFBs) are electrochemical energy storage and conversion devices that show great promise for grid-scale stationary application due to their simplicity, durability and ability to decouple energy capacity and power. The energy capacity is proportional to the volume of redox-active species containing electrolyte solution stored in external tanks and the power is proportional to the total electrode area in the stack [1]. They operate by flowing the redox species, traditionally metal ions dissolved in an aqueous solution, into a porous electrode, on the surface of which the electron transfer occurs. In addition to metal-based aqueous chemistry, gaseous reactants can be used, and organic molecules in non-aqueous electrolytes have achieved a lot of attention recently [2], particularly quinone based chemistry [3], Typical electrode materials employed in RFBs take the form of carbonised felts, woven mats or fibrous paper, with all materials being highly porous and made from conductive carbon fibers or strands [4]. The diffusion properties and flow characteristics of the porous media employed as electrodes can have a large bearing on the performance of the flow battery, influencing the mass transport of the active species, the pressure drop (and subsequent parasitic pumping power losses), and areas of stagnation in the electrode. These characteristics are strongly coupled to microstructural properties such as porosity, pore size and shape, tortuosity

and fiber diameter, and thus there is a desire to fully understand the microstructure of porous media in 3D [5].

The recent advances in X-ray computed tomography (CT) have allowed characterisation of the microstructure of many electrochemical devices such as lithium-ion batteries [6-11], solid oxide fuel cells [12-19], polymer electrolyte fuel cells [20-26], supercapacitors [27, 28] and, more recently, RFBs [29-33]. The application of tomographic images in the study of porous media has the benefit of allowing numerical simulations to be conducted directly on the actual structures represented in the images, and therefore allowing prediction of the material's performance based on its microstructural properties. For this reason, there has been a recent surge in the desire to acquire high quality X-ray CT data of porous media [5, 32-41].

Since RFB performance depends directly on electrode structure, there is a strong drive to produce structurally novel materials with improvfed performance. Electrospinning is a good technique for creating fibrous materials with a variety of structures, since there are various adjustable parameters in the process [42]. Nano- and micro-fibers are 'spun' from a polymer-containing solution onto a target with a large potential difference, typically over 10 kV. The technique has been used to generate materials for lithium-ion battery separators [43-45], supercapacitors [46-48], fuel cells [49, 50] and, recently, RFBs [34, 51-53]. The advantage of using electrospun fibers in these devices is that it allows for small fiber diameters, which increase the specific surface area, and with careful variation of various parameters can allow control of porosity, fiber size and alignment. However, the small fiber sizes typically produced (less than 1 µm) make characterisation of electrospun fibrous mats difficult, with many parameters often estimated from two-dimensional analyses such as SEM [46]. Consequently porosity measurements on thin mats have proven challenging [54].

Recently, the authors demonstrated the successful application of X-ray micro-CT to electrospun fibrous materials, producing virtual volumes of the mats for detailed computer

modelling and assessment of the structural heterogeneity within the full thickness of the materials [34, 52]. The electrodes used in this study were composed of relatively large fiber sizes and displayed inhomogeneity through the thickness of the mat. Thus, they were able to be imaged with sufficient resolution using micro-CT at an effective pixel size of around 400 nm and required the large field of view obtainable at this resolution to study their structural heterogeneity through the entire thickness of the material. However, towards the smaller end of the distribution of diameters, there were some fibers of a size that was close to the resolution limit of the scan parameters. Additionally, more homogenous mats with smaller fibers might be desired in order to increase specific surface area and produce more evenly distributed flow throughout the electrode. For these materials, an improved resolution and sample preparation methodology must be developed in order to image the fibers with sufficient accuracy for reliable parameter determination from the 3D X-ray CT data. A higher specific surface area can be achieved by reducing the size of the fibers and reducing the porosity (as shown by the filament analogue model [55]) and is desired in order to increase the number of reaction sites in the electrode, and therefore the reaction rate. However, through Darcy's law and the Carmen-Kozeny correlation of permeability in fibrous material [56, 57], it is known that the permeability coefficient (and therefore the mass transport) rapidly decreases with reducing fiber size or porosity, and therefore increasing specific surface area. Therefore, the drive to produce smaller fibers with methods such as electrospinning could come at the cost of reduced permeability and increased parasitic pumping losses in the system. For this reason, the introduction of a degree of alignment into the electrode is an attractive prospect; as RFBs largely employ directional flow, directional alignment could permit high permeability in that direction while retaining the benefit of increased specific surface area through smaller fibers.

Here we present, for the first time known to the authors, high resolution X-ray imaging of three different electrospun electrodes using a lab nano-CT system and the subsequent

extraction of parameters from the highly resolved data. All three electrodes are composed of the same material; however, they represent three very different microstructures; EE-H (heterogeneous) has varied fiber size, EE-C (consistent) has controlled and small fiber size, and EE-A (alligned) as a degree of alignment of the fibers. The merits of the trade-off between resolution and sample volume will also be discussed, along with the computationally-extracted parameters and properties of each electrode.

2. Methods

2.1 Material Preparation

The electrospun materials were generated on a custom built electrospinner [34, 51]. The spin dope was pumped by a syringe pump through a connecting tube to a grounded needle. A large 4-inch rotating drum was used as the collector, and was charged by a negative polarity power supply (Glassman, MJ20N0400-11) to create the high voltage field necessary for electrospinning. The needle was connected to a linear motion actuator that rastered constantly throughout the electrospinning process at a speed of 5 mm s^{-1} to ensure consistent material properties and spinning conditions over the width of the material. The spin dope was pumped at a rate of 0.5-0.8 mL hr^{-1} through a 16-gauge stainless steel needle placed 15 cm from the collector. The collector was initially held at -15 kV but this could be adjusted throughout to improve the spinning characteristics.

The spin dope consisted of polyacrylonitrile (PAN) (Sigma, MW 150,000) dissolved at 12 wt% in anhydrous N,N-dimethylformamide (Sigma, 99.8%). PAN is the polymer of choice when the material is to be carbonized (necessary for electrical conduction in the electrodes), since it has a high yield and maintains its shape and size [58]. The concentration of 12 wt% was chosen as it generates materials most suitable for flow battery electrodes; specifically, materials with large fibers. The fiber size is largely determined by the concentration of the spin dope,

with higher concentrations yielding larger fibers. Concentrations higher than 12 wt% are possible; however, pumping the solution can become very difficult as the viscosity increases significantly. In addition to this, at higher concentrations the electrospinning solution tends to become very unstable, leading to inconsistent materials.

The materials presented here represent three different methods of operating the electrospinner which result in three distinct morphologies, which will be referred to as EE-H, EE-C, and EE-A, referring to Heterogeneous, Consistent, and Aligned materials, respectively. For the EE-H sample, electrospinning conditions were set at the beginning and held constant throughout the processes (about 12 hours for all cases). Electrospinning is a dynamic process, however, so maintaining constant conditions results in an inconsistent material with a heterogeneous distribution of properties. For example, it is driven by a potential field between the spin dope at the needle and the collector; however, as the process continues there is a continual build-up of an electrically insulating material on the surface, affecting the electric field. Previous studies on the morphology of these materials showed significant variability in material properties throughout [34]. By contrast, EE-C was made using a more refined method. The electrospinning process was closely monitored during the controlled process, and any deviation from ideal operation was corrected for. Typically, this would mean gradually lowering the flowrate of the spin dope as well as adjusting the applied voltage between the needle and collector to account for the changing electrostatic conditions. The EE-A sample was also produced using this closely monitored approached, with the additional feature that the collector drum was rotated rapidly. This had the effect of adding anisotropy in the materials by increasing the velocity of the rotating drum collector from the nominal 0.5 m s^{-1} to 7 m s^{-1} as previously demonstrated [59], resulting in a degree of alignment in the direction of the fibers.

After electrospinning, the PAN fibers were carbonized to make electrically conductive materials suitable for use as flow battery electrodes. This carbonization was performed in an

inert environment at 1050 °C for 40 minutes. More details about the carbonization process can be found elsewhere [51].

2.2 Sample Preparation

Due to the high resolution and low energy of the lab nano-CT system, small samples must be carefully prepared in order to allow sufficient transmission of X-rays [16]. Thus, small segments of the electrodes were glued to a dowel with epoxy and then lathed into pillars of around 150-200 µm diameter using a laser micromachining system (A-series, Oxford Lasers) using a method described by Bailey et al. [60].. As the largest field-of-view achievable in the nano-CT instrument is 65 µm, all scans are internal, which means that any superficial laser damage to the fibers is not included in the volume of the scan. The definition of the axes and planes used in this work is as follows: z being the vertical or through-plane direction, perpendicular to the surface plane of the electrode mat and representing the thickness of the electrode, and the xy plane being normal to the surface plane of the electrode. As cylindrical samples were created by the laser lathe, the distinction between the x and y directions is random and arbitrary. In the case of the aligned material, EE-A, the virtual volume was rotated after the scan, such that, to eye, the alignment direction was parallel to x and perpendicular to y.

2.3 Nano X-ray Computed Tomography and Image Processing

A lab-based nano-CT instrument (Zeiss Xradia Ultra 810, Carl Zeiss Inc., Pleasanton, CA) was used to acquire the X-ray images, containing a Cr anode source with an accelerating voltage of 35 kV, producing a quasi-monochromatic beam at the Cr-Kα emission line of 5.4 keV. A Fresnel zone plate was employed as the objective element to produce a magnified image on a 1024^2 pixel CCD detector and images were acquired in large field-of-view mode with no binning, resulting in a pixel size of ca. 63 nm and a field-of-view of ca. 65 µm. The sample was rotated through 180° and radiographs collected at discrete angular intervals, the number

and exposure time of the radiographs varied for each scan and details of the scan parameters can be found in Table 1.

The radiographs were then reconstructed with proprietary software (XMReconstructor, Carl Zeiss Inc.) using a parallel beam reconstruction algorithm. Each electrode was scanned in Zernike phase contrast mode where a Au phase ring is inserted in the back focal plane of the objective and shifts the un-diffracted component of the beam, resulting in negative Zernike phase contrast (more details of which can be found in the paper of Tkachuk et al. [61]). EE-C was also scanned in absorption contrast mode and combined with the phase contrast image using Dual Scan Contrast Visualizer software (Zeiss) with a 50/50 contribution from each image using a method described by Taiwo et al [37]. The result of this contrast combination can be seen in Figure 1, and provides the benefit of both the well-defined fiber edges from the phase contrast image and the reduced background streaking of the absorption image. The scans for EE-H and EE-A did not require this, with the phase contrast image being sufficient for clear distinction between the fiber and pore phases. A non-local means filter was also applied to the EE-C sample, but was not necessary for accurate segmentation of the other two data sets. This could be a result of the sample preparation. For all scans, the tomogram represents a volume that is an internal fraction of the total sample volume (the data represents roughly 65^3 μm^3 while the pillars are between 150-200 µm in diameter), due to laser lathed pillars becoming prone to delamination and destruction below this size. This gives the background, or pore phase, a slightly mottled noise effect that can be removed in segmentation, as described later. As close monitoring of the laser lathing process was required to prevent damage to the electrode via delamination, for the EE-C sample the process was halted slightly earlier in a conservative manner. This resulted in a slightly larger sample than for EE-H and EE-A, and therefore a higher attenuation of the x-rays and more noise in the background or air phase. However, imaging in Zernike phase contrast has the effect of producing dark and light 'halo' effects

around the outside and inside of the fiber phase, respectively, which can be seen quite clearly in the *xz* orthoslices of the greyscale reconstructed data (Figures 3-5 a) [37, 62]. Though this can be removed through the use of computer algorithms[63], it is not necessary in the case of the relatively small fibers imaged in this study, and in fact his serves to highlight the fiber phase and makes the mottled background less problematic for accurate segmentation.

A micro-CT scan of the whole thickness of the EE-A electrode was also carried out to assess the homogeneity of the sample. This scan was conducted using a Zeiss Xradia Versa 520 micro-CT instrument (Carl Zeiss XRM, Pleasanton, CA), operating with a source voltage of 40 kV and acquiring 1601 radiographs of 46 s exposure over a sample rotation of 360°. The instrument utilizes a two-stage magnification system, coupling geometrical magnification with an optically coupled scintillator, and is described elsewhere [62]. A 20 × objective lens was used, resulting in a pixel size of 312 nm.
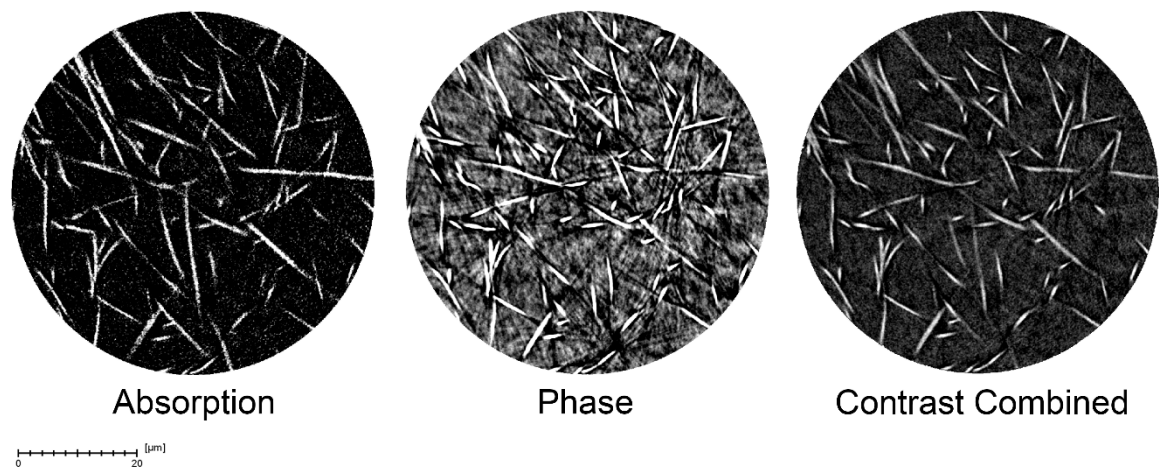

Figure 1: *xy* orthoslices of EE-C imaged using nano-CT in the absorption (left) and Zernike phase contrast (middle) modes. Both data sets are combined with a 50/50 influence of each to produce a contrast-combined image (right)

The grey-scale reconstructed volume was then segmented into a binary image using Avizo Fire software (Thermo Fisher Scientific, Waltham, MA, USA) using a combination of thresholding based on pixel value, watershed algorithms and reduction of background noise by removing isolated islands. Voxels are then designated as either 'fiber' or 'pore' for the whole

cylindrical volume of the scan. These binarised data sets were used for the various visualisations and extraction of parameters presented below, with the Aviso module 'label analysis' used to calculate the 3D surface area and volume of each material on the voxel image (with no meshing or creation of a simplified surface). For more computationally intensive modelling, 500^3 voxel sub-volumes were extracted from the whole data. In the case of the EE-C and EE-A electrodes, where the fiber size was consistent throughout the material, the sub-volume was extracted from the centre of the sample. For the EE-H electrode, two locations were chosen; one which incorporated the large fiber and the void adjacent to it, and one that avoided this heterogeneity in an attempt to capture only the smaller and more consistent fibers. The location of these sub-volumes is shown in Figure 8 (a), and orthogonal 3D views of all four sub-volumes are shown in Figure 8 (b).

The MATLAB application TauFactor [64] was used to predict the tortuosity factor on these 500^3 voxel sub-volumes in the *x*, *y* and *z* directions, in both the pore phase and the fiber phase. TauFactor estimates the tortuosity of a phase by simulating Fickian diffusion and determining an effective diffusion coefficient, more details of which can be found in the work of Cooper et al.[64] The ImageJ [65] software package, and in particular the 'Beat' plugin [66], was used to calculate the 3D continuous pore size distribution, again applied to the 500^3 voxel sub-volumes to reduce computational demands. This process uses the local thickness method, which assigns each voxel the radius of the largest sphere that can fit entirely within the pore space and overlaps the voxel (note that this differs from the standard distance transform, which gives the largest sphere that is centred on each voxel). The resulting grey-scale image was then used for visualisation of the pores shown in Figure 9, with a colour map applied to the grey-scale values (each pixel's grey value being equivalent to the value of the radius of the sphere). More detail on this method can be found in the paper of Münch and Holzer [66]. The same method was also applied to the fiber phase to assess the local fiber diameter. In this case, the

sphere radius was increased in ½ voxel steps, with only fibers of four pixels diameter and above considered.

Table 1 Scan parameters

Sample	Imaging Mode	No. Projections	Exposure time (s)	Voxel Size (nm)
EE-H	Phase	2001	40	63
EE-C	Phase	1601	24	63
EE-C	Absorption	1601	7	63
EE-A	Phase	1601	45	63
EE-A	20× (Versa 520)	1601	46	312

2.4 Permeability

The permeability coefficient for each material was determined by simulating viscous pressure driven flow using the Lattice Boltzmann Method (LBM). These simulations were implemented using the open-source LB solver Sailfish FD [67] using a 3D D3Q19 single relaxation time model with the standard Bhatangar-Gross-Krook (BGK) collision operator. Initially the velocity was held at zero everywhere and the fluid movement was initialized by applying a fixed pressure gradient between the inlet and the outlet [68]. The permeability coefficient for a material should be independent of flow rate or pressure drop. The applied force was varied across several orders of magnitude to ensure the permeability coefficient was unchanged. This was found in all cases.

The electrospinning process produces planar materials, leading to a certain degree of alignment in the thru-plane (z) direction. One would expect the permeability in this direction to be significantly lower than the in-plane directions, as this flow is perpendicular to fibers. For unaligned materials (EE-C and EE-H) the fibers in-plane are isotropic and there should not be

a significant difference in the permeability tensor's x and y components [59]. Similarly, for aligned electrospun media (EE-A), the alignment of the fibers in-plane should cause a significant divergence in the in-plane components. For flow parallel to the fibers the permeability should be much larger as there are very few obstructions to the flow, while in the other direction the permeability should be similar to the thru-plane permeability for the same reason - the flow is largely perpendicular to fibers. In the case of EE-A flow in the x-direction is parallel to the fibers and flow in the y-direction is perpendicular. An example showing the results of the LBM study for flow perpendicular to the fiber alignment can be seen in Figure 2.
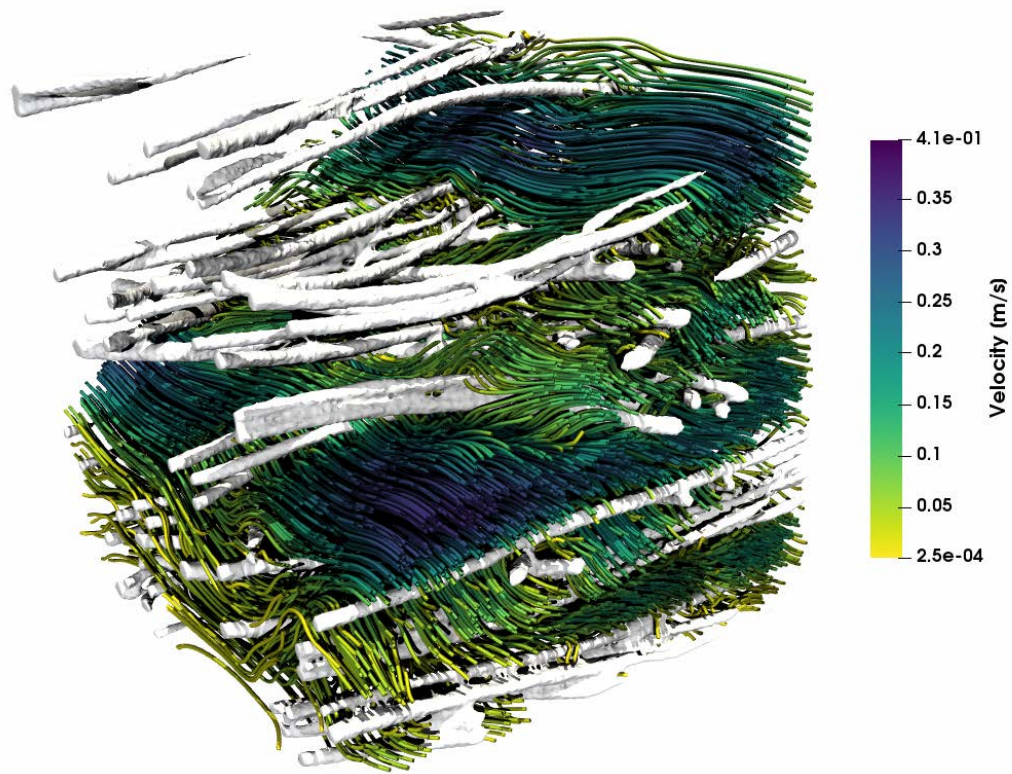
Figure 2 Example of LBM results showing the streamlines (coloured) for flow perpendicular to the fibers (white) in the EE-A material

3. Results

3.1 Imaging

Nano-tomographic images of the electrospun electrodes can be seen for EE-H, EE-C and EE-A in Figure 3, Figure 4 and Figure 5, respectively. The morphological difference between the heterogeneous electrode, EE-H (Figure 3), and the electrodes produced with fiber control, EE-C and EE-A (Figure 4 and Figure 5, respectively) is stark, with the variation in fiber size and the pore void created around the single extremely large fiber being clear in the nano-scale X-ray-CT. It is also possible to see evidence of bundling of multiple fibers (Figure 3 b and c) and internal porosity in the larger fiber (Figure 3 a and d). This material was previously studied using a micro-CT instrument [34] (specifically, the electrode denoted EE-H here is the '12 wt% Carbonised' material in Kok et al. 2018) with a voxel size of around 400 nm – sufficient to resolve the larger fibers and bundled fibers, as well as to show the fiber variation throughout the thickness of the electrode mat. Given the structural heterogeneity in these uncontrolled materials, it is important to obtain a sufficient scan volume such that the effect of changing porosity, as well as pore and fiber size, can be assessed throughout the thickness of the electrode (representing fiber deposition over time). However, for X-ray tomographic studies, and indeed all imaging studies, there is always a trade-off between voxel size or resolution, and sample volume, or field-of-view – the higher the resolution, the smaller the volume of the sample that can be scanned. In the case of the nano-CT instrument used in this study, the scan volume is around 65^3 µm. Clearly, the heterogeneities of EE-H, both based on the location of the scan in the electrode, and the large variation in fiber size throughout, mean that the smaller sample volume of the nano-CT results in an unrepresentative volume of the electrode. Conversely, some of the smaller features and fibers are difficult to resolve at the scale of the micro-CT and so some information is lost.

For the previous study [34], the feature size was reasonably large, and the variation throughout the electrode mats sufficiently extensive, that the lower resolution but larger field-of-view was deemed more suitable for these materials. However, on controlling the electrospinning conditions and producing materials with a more controlled and smaller fiber morphology (EE-C and EE-A), the limits of the resolution of the micro-CT are approached. Figure 6 shows an example micro-CT scan of EE-A, with the *xz* orthoslice (left) showing consistent fiber size throughout the thickness of the electrode (epoxy resin has seeped into the lower portion of the electrode during sample preparation, but it is nonetheless possible to observe the consistency in morphology throughout). The voxel size of 312 nm, however, is too large to properly resolve the fibers, meaning that there are only 1-3 voxels covering the fiber diameter. This leads to the low resolution seen in the magnified view of the *xy* orthoslice (Figure 6, top right) and subsequent poor segmentation of the data for the 3D representation (Figure 6, bottom right). Therefore, not only is micro-CT deemed too low resolution for these materials, nano-CT (with a smaller sample volume) is deemed representative where the fiber size is controlled throughout. Though the sample volume of EE-H (Figure 3) is not representative of the electrode as a whole, the increased resolution of the nano-CT approach can still give unprecedented insights into the properties of these materials, with features such as the bundling, void creation and internal porosity of large fibers not accessible in the micro-CT resolution.

As has already been mentioned, the electrodes with a degree of control in their synthesis (EE-C and EE-A) display smaller fiber size and more consistent fiber morphology, as can be seen in the *xy* orthoslices at different *z* positions (Figure 4 Figure 5, b-d). The volume specific surface area of the fibers (calculated in 3D) for both controlled electrodes is 7.1 μm^{-1}, whereas it is 3.0 μm^{-1} for EE-H, although, naturally, the large fiber in the EE-H volume clearly influences this. A sub-volume excluding this fiber, extracted for analyses later in this work,

gave a volume-specific surface area of 5.4 μm^{-1}, still lower than that of the smaller controlled fibers of EE-C and EE-A (see Figure 8 a for the location of this sub-volume, EE-H2). The porosity calculated from the volume fraction of the whole scan is 82%, 93% and 96% for EE-H, EE-C and EE-A, respectively. The porosity of the aligned electrode (EE-A) is higher than that expected from similar materials made using the same process [59] from experiment, which could be due to slight delamination of the sample during preparation of the laser-lathed pillar. This is because the degree of alignment of the fibers in this material leads to less crosslinking between layers in the *xy*-plane and means these electrodes are more prone to delamination. The porosity of the EE-H electrode is lower than the value previously obtained from micro-CT (89.5%), again highlighting that this small volume including the large fiber is not representative; the porosity of the sub-volume EE-H2, largely excluding the large fiber and void, is 86%, which falls in the expected range for this material

In order to better visualise the degree of alignment in the electrodes, a projection of the grey-scale data in the *z*-direction was carried out over a distance of 200 pixels, the results of which are shown in Figure 7. There is clearly an overall prevalence of alignment of the majority of the fibers in the *x*-direction for the EE-A electrode, (and a minority in the *y*-direction), with the other two materials showing no overall preference for fiber alignment.

For all samples, a high-quality scan was achieved with unprecedented detail for such small electrospun fibers. This allowed relatively trivial segmentation of the data to provide accurate binarised volumes, with EE-A requiring only simple thresholding combined with island removal, EE-C employing a non-local means filter to remove background noise and, EE-H using a watershed algorithm. However, this was largely due to the one large fiber showing a reduced internal grey-value in Zernike phase contrast mode – had this scan also used contrast combination with an absorption phase image, as with EE-C, see Figure 1, the watershed approach would probably not have been necessary. The combination of careful sample

preparation and nano-CT resolution has enabled, for the first time, clearly resolved imaging of sub-micron electrospun electrodes in the lab.
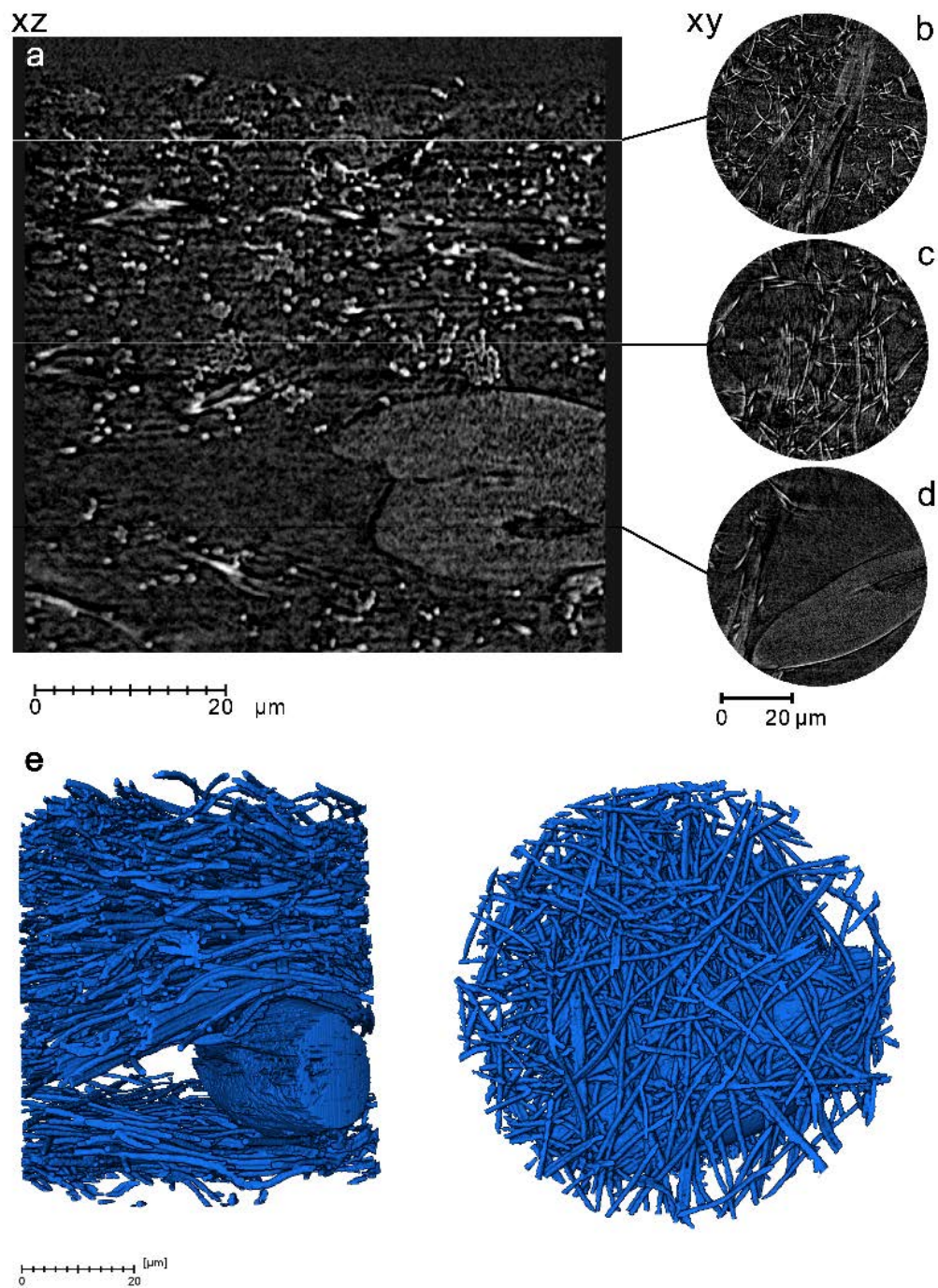

Figure 3: Nano-CT images of the EE-H electrode, showing a cross-sectional orthoslice through the thickness of the sample in the *xz*-plane (a), three *xy* orthoslices at different *z* distances in the sample (b-d) and a 3D rendering of the segmented grey-scale data (e) in the in-plane (left) and through-plane (right) views.
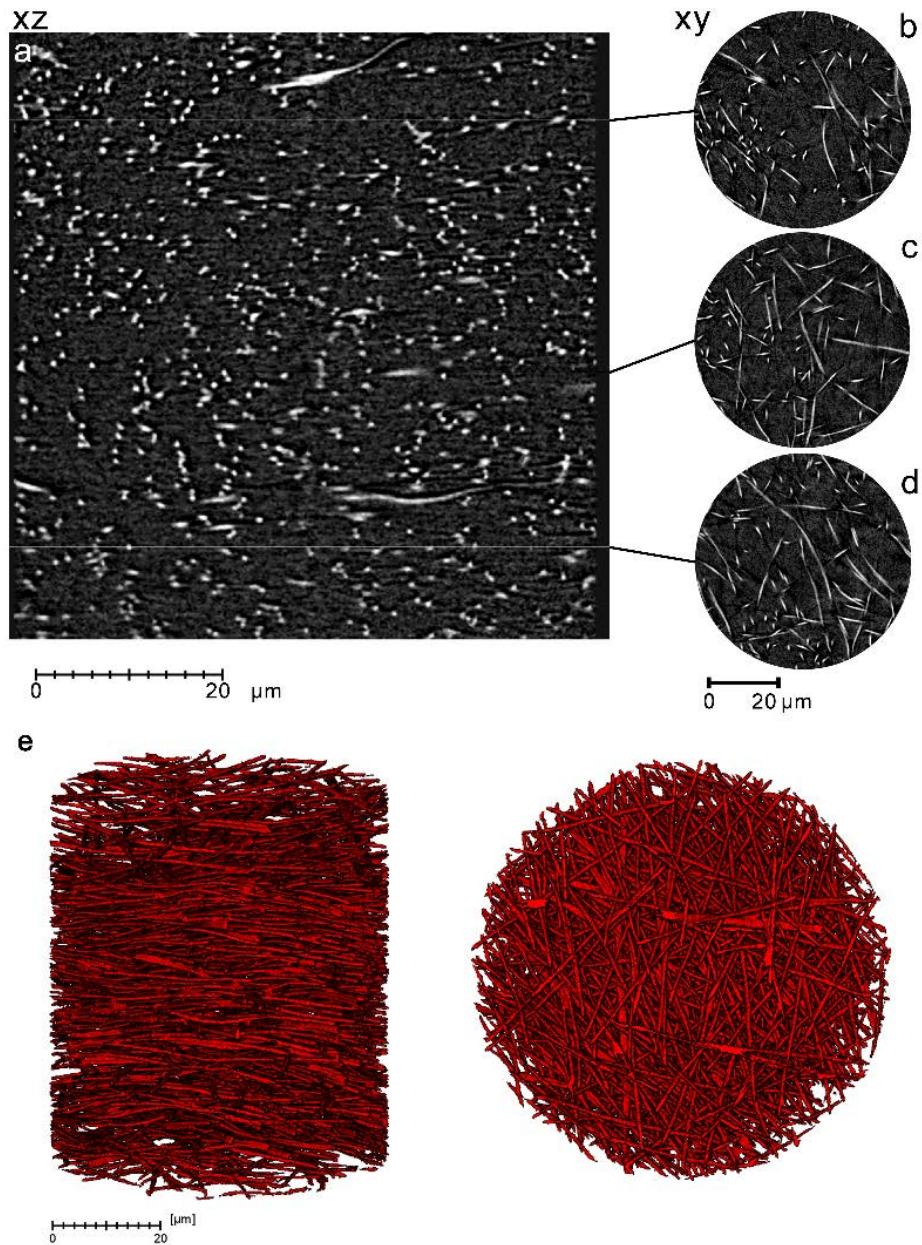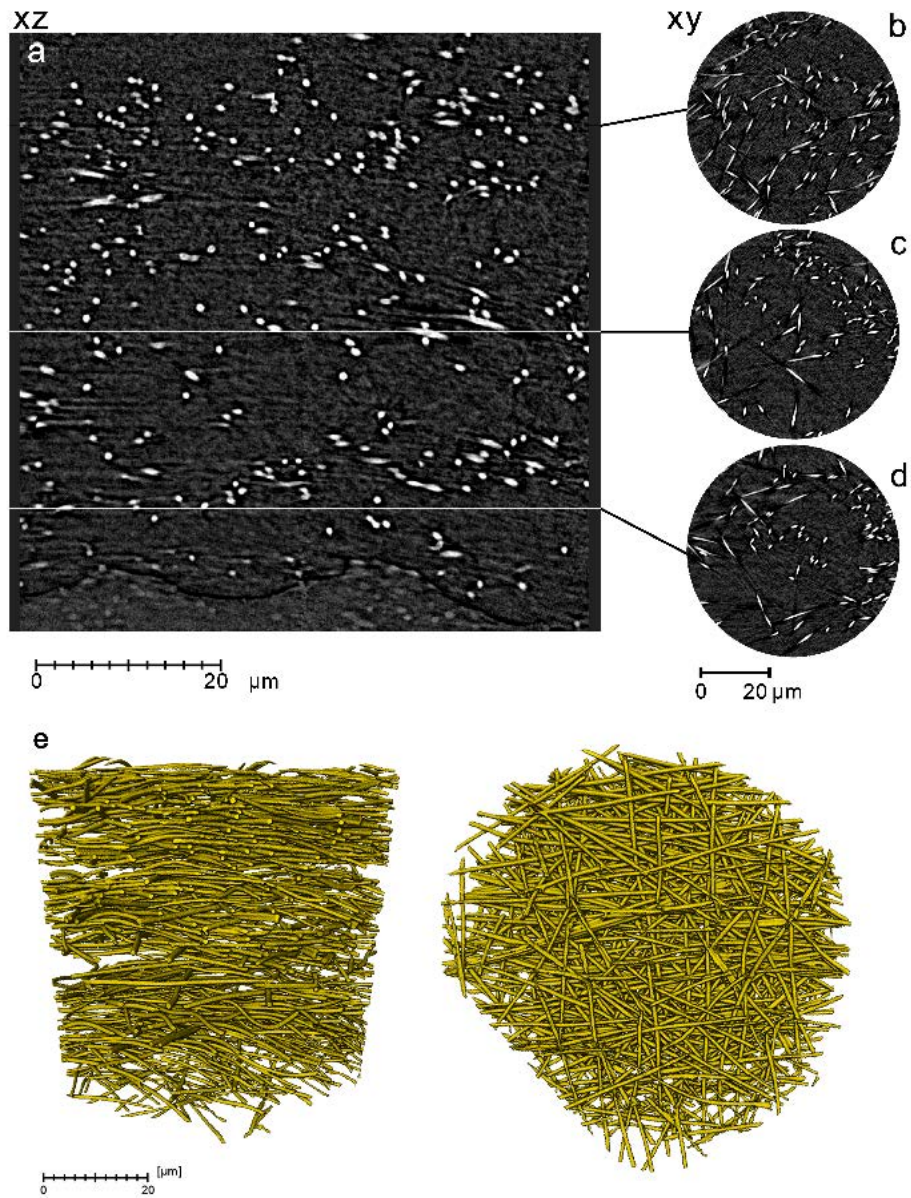
Figure 4: Nano-CT images of the EE-C electrode, showing a cross-sectional orthoslice through the thickness of the sample in the *xz*-plane (a), three *xy* orthoslices at different *z* distances in the sample (b-d) and a 3D rendering of the segmented grey-scale data (e) in the in-plane (left) and through-plane (right) views.
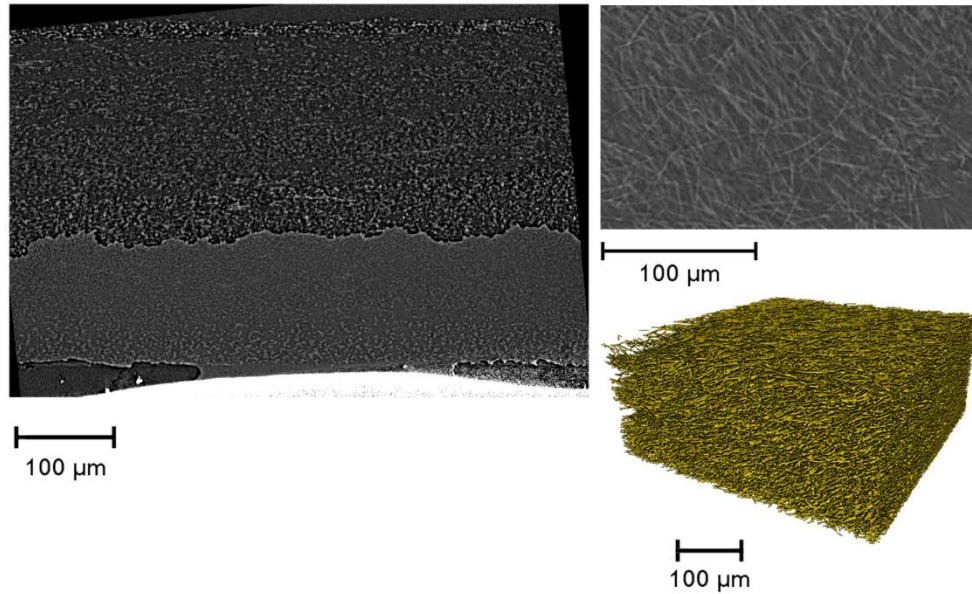
Figure 5: Nano-CT images of the EE-A electrode, showing a cross-sectional orthoslice through the thickness of the sample in the *xz*-plane (a), three *xy* orthoslices at different *z* distances in the sample (b-d) and a 3D rendering of the segmented grey-scale data (e) in the in-plane (left) and through-plane (right) views.

Figure 6: Micro-CT of the EE-A electrode, obtained with a voxel size of 312 nm. The fiber size is seen to be consistent throughout the thickness of the electrode in the cross-sectional *xz* orthoslice (left), though the resolution is not high enough to fully resolve the fiber morphology in the *xy* magnified orthoslice (top right). This leads to poor segmentation and 3D rendering of the fibers (bottom right). Epoxy can be seen to have seeped into the bottom third of the electrode during sample preparation (left).
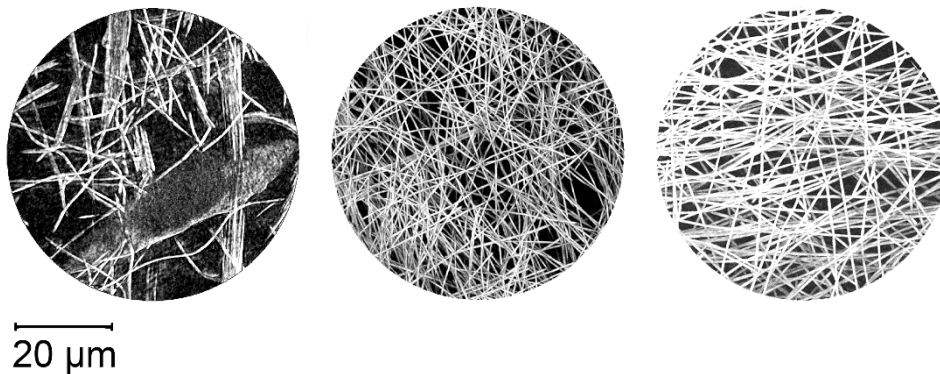

Figure 7: Projections of *xy* orthoslices by summing the grey-scale datasets in the *z*-direction through a distance of 200 pixels showing the arrangement of the fibers in the EE-H (left), EE-C (middle) and EE-A electrodes. Preferential alignment of the majority of the fibers in the *x*-direction, and the minority of the fibers in the *y*-direction can be seen for the EE-A electrode.

3.2 Tortuosity Factor

As with any porous media, the tortuosity of the electrodes in 3D is a highly useful parameter in comparing the diffusion characteristics of the materials. The MATLAB application TauFactor [64] was used to determine the tortuosity factor, τ, for each electrode in

the pore phase. τ is a dimensionless number that represents the extent to which a path deviates from its straight-line distance, with a larger value of τ representing a more tortuous path [5, 36]. Due to the computational demands of these simulations, 500^3 voxel samples (around 32^3 μm^3 volume) were extracted from the full data sets, from the middle of the volume for EE-C and EE-A, and from two different locations for EE-H. These locations are denoted EE-H1 and EE-H2 and were chosen to deliberately include and exclude the large fiber mass, respectively. The location of these sub-volumes is shown in Figure 8 (a), and orthogonal views of every sub-volume and their corresponding tortuosity factor is shown in Figure 8 (b). In the first instance, only the sub-volumes that represent reasonably homogenous materials will be considered, that is EE-H2, EE-C and EE-A. As the mats are formed by successive deposition of layers of fibers in the xy-plane, increasing in thickness in the z-direction, τ z can be considered a reasonably similar comparison for each material. Figure 8 (b) shows that the tortuosity factor decreases in the z-direction with increasing porosity, as might be expected. EE-H2, the sample with the largest fibers and least control, also has the largest tortuosity factor in this direction. In all cases, the tortuosity factor in the x- or y-directions is lower than the corresponding z-direction for the same electrode. There is a notable difference in the tortuosity factor in the x- and y-direction for the aligned material, EE-A, with the former direction having a lower tortuosity factor due to the alignment of the fibers in the x-direction. This is not the case for EE-C where there is no degree of alignment.

EE-H1 is naturally highly affected by the presence of the large fiber. It is the only sub-volume to display a larger in-plane tortuosity factor than its through-plane value, given the sideways orientation of the large fiber in the y-direction. This indicates that local diffusion pathways through this material could be highly directionally dependant near a large fiber.

The tortuosity simulations were also carried out on the fiber phase, as this represents the electrical conductivity of the solid phase. Though there are many factors that could

influence the actual conduction pathways in electrospun electrodes (such as whether they are beneath the channel or the land of a current collector, internal anisotropy of the fibers and compression) the through-flow configuration used in the TauFactor application is used in this analysis as a way to compare the alignment of the fibers, and the effect this could have on through-flow conductivity in a qualitative manner. For all materials, the simulation did not converge in the z-direction, indicating little to no contact between the fibers in different xy-planes, at least within the small domain used for these simulations. Though this is not the case over the electrode as a whole, where some fibers will leave the xy-plane and make contact between the planes, and contact would greatly increase if the materials were imaged under compression, it reflects the reality that the through-plane conductivity in fibrous porous media is often significantly lower than the in-plane conductivity [69].

Figure 8 (c) shows normalised flux maps in the xy-plane, projected (summed) in the z-direction for EE-C (top) and EE-A (bottom). These maps give a qualitative idea of regions of high flux (brighter colour) of the diffusing element when initiated in either the y-direction (left) or the x-direction (right). In the case of the fiber phase, this flux represents the electrical conductivity, with brighter regions showing points of high electron flow, based on a less tortuous, and therefore more favourable, pathway for current flow. It is clear from these flux maps that the unaligned electrode, EE-C, has a reasonably similar flux in both directions; whereas the aligned electrode, EE-A, has only a few conductive pathways in the y-direction compared to many in the x-direction, the direction of alignment. Comparison of this with the projections in Figure 7 highlights the fact that there are fewer fibers aligned in the y-direction compared with the x-direction. All the extracted tortuosity factors are summarised in Table 3; EE-H1 is, again, highly influenced by the alignment of the large fiber, with the tortuosity factor in the y-direction being nearly an order of magnitude higher than that of the x-direction. The influence of the large fiber in EE-H 1 is also highlighted in the representative volume analysis

shown in Figure 8 (d) – all other electrodes show a convergence of the pore/fiber phase volume fraction with a small (< 0.5) fraction of the 500^3 voxel sub volume, whereas the EE-H 1 sub volume does not converge, showing that this sub volume is not large enough to be representative of the highly heterogeneous material.
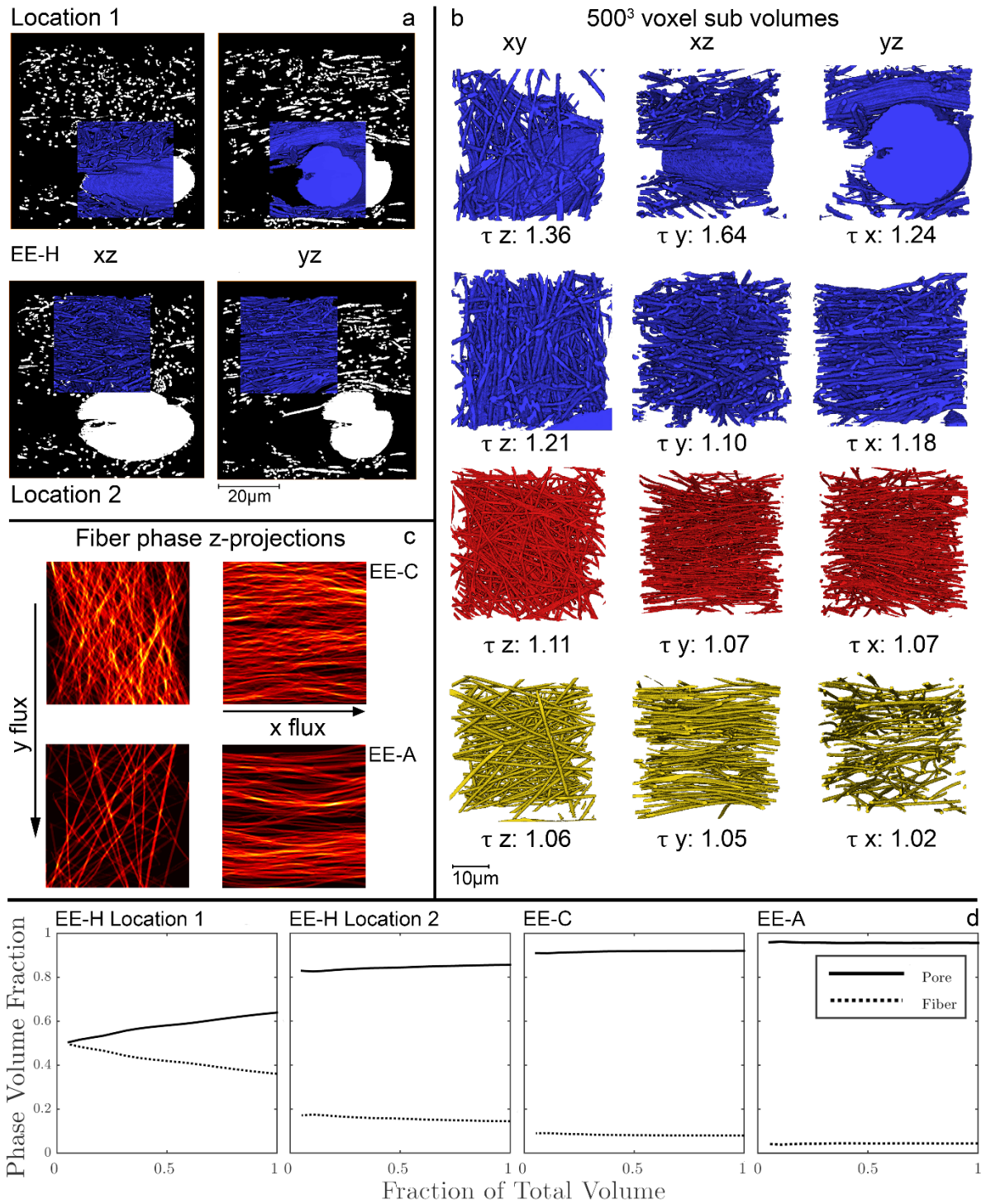
Figure 8: Tortuosity calculations: 500³ voxel sub-volumes were extracted from the full data sets for use in the tortuosity calculations from two different locations for M1-V (blue) shown in (a) – location 1 including the large fiber and location 2 avoiding the large fiber. The tortuosity factor of the pore phase is shown in (b) for each direction: the *xy*-plane (*z*-direction, left), the *xz*-plane (*y*-direction, middle) and the *yz*-plane (*x*-direction, right), and for each material: M1-V location 1 (blue, top), M1-V location 2 (blue, bottom), M2-C (red) and M3-A (yellow). The flux in the fiber phase is shown in (c) for M2-C (top) and M3-A (bottom) via projection summations of the *xy*-planes in the *z*-direction. The left two images represent the through-plane (*xz*-plane) flux in the *y*-direction and the right two images represent the

through-plane (*yz*-plane) flux in the *x*-direction. The colour scale in (c) is normalised to the histogram for each material and thus represents a qualitative visualisation of the flux only. Representative volume analysis was performed on TauFactor using a uniform shrink of the volume, and the pore/fiber phase volume fraction as a function of the fraction of the total 500³ subvolumes is shown in (d). All subvolumes converge with a small fraction of the total volume (< 0.5) except EE-H 1, showing that the presence of a large fiber in the volume makes it unrepresentative.

3.3 Pore Size distribution

The same 500^3 voxel sub-volumes used in the tortuosity simulations were used to calculate a continuous 3D pore size distribution using the 'Beat' plugin of ImageJ. More information on this method can be found in the methods section and in the paper of Münch and Holzer [66]. The pore size distributions for the sub-volumes are shown in the histograms of Figure 9 (left), and the pores are also visualised in 3D in Figure 9 (right). Average pore sizes of 3.61 µm, 1.58 µm, 1.53 µm and 2.57 µm were calculated for EE-H1, EE-H2, EE-C and EE-A, respectively, with the void space adjacent to the large fiber in EE-H1 skewing the pore size towards higher values, and the delamination experienced by EE-A in sample preparation leading to slightly larger pores than in the other electrodes.
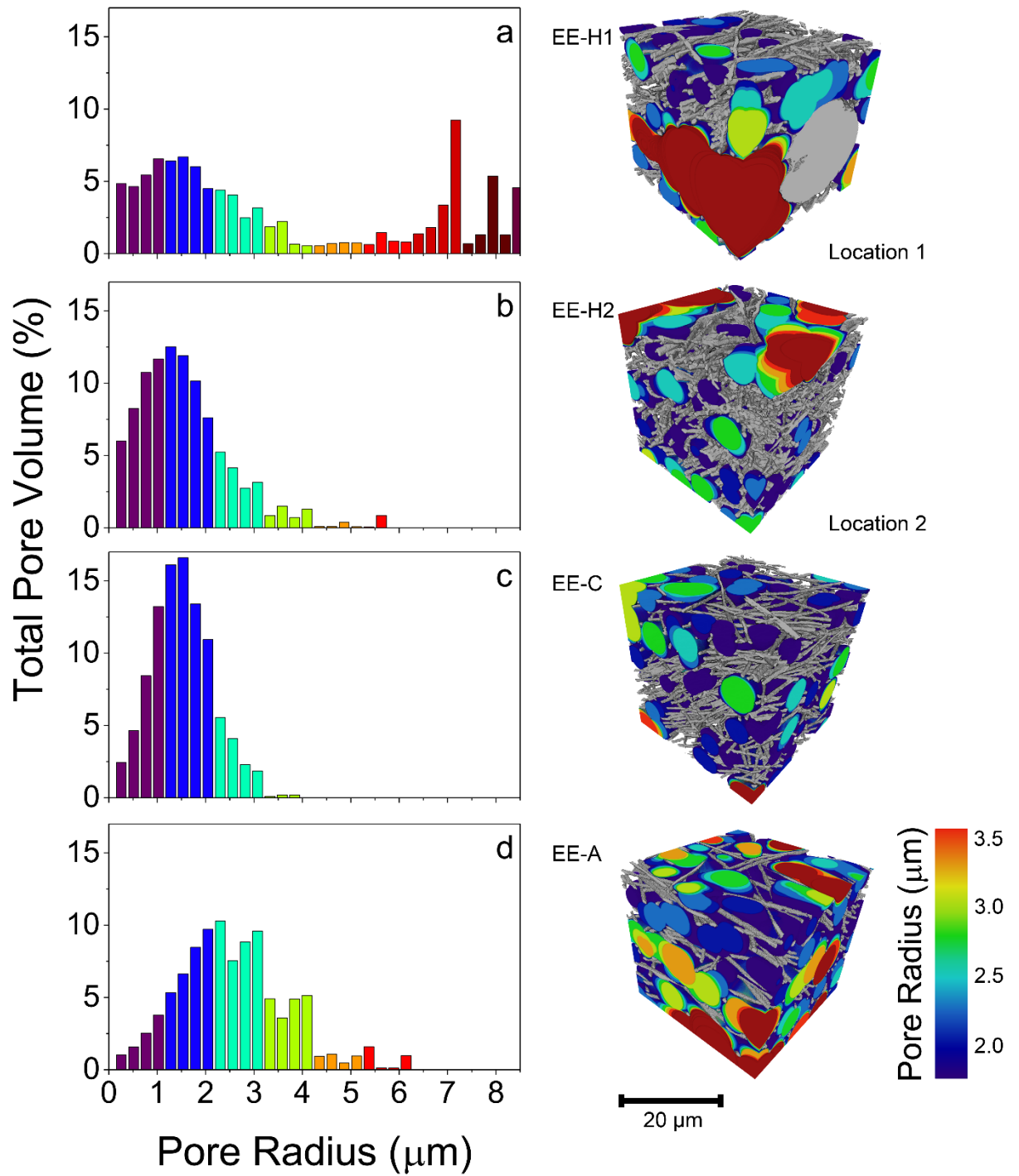
Figure 9: Pore size distribution of the 500³ voxel sub-volumes showing the histograms for EE-H1 (a), EE-H2 (b), EE-C (c) and EE-A (d), left, and the location of the pores of varying size in 3D, right. The colour scale represents the radius of the pore by the largest sphere in the pore phase that it is possible to grow at that voxel. Pores below 1.5 µm radius have been removed in the visualisations (right) for clarity.

3.4 Fiber Diameter

The same method for the continuous pore size distribution was also applied to the fiber phase to produce a localised fiber diameter. Due to the smaller size of the fibers compared with the pores, the whole volume was able to be used in these simulations. Figure 10 shows the fiber diameter distribution (left) and colourised 3D and 2D orthoslice representations of the fiber diameter (right). An average fiber diameter of 636 nm, 477 nm and 469 nm was calculated for EE-H, EE-C and EE-A, respectively, though for the EE-H electrode this value excludes the single anomalously large fiber present in the volume. Including the large fiber gives an average fiber diameter of 4 µm for the EE-H electrode.

As expected from the grey-scale visualisation, EE-H has larger fibers and, within error, the two controlled electrodes, EE-C and EE-A, have the same fiber size. There is no obvious variation of fiber size throughout the sample, with narrow distributions in diameter shown for both controlled electrodes. Importantly, the average fiber diameters for the controlled electrodes are both under 500 nm, meaning that if analysis by micro-CT was to be attempted with the same scan parameters as in Figure 6, the average fiber diameter would be less than two pixels across. The pixel size of around 63 nm in the nano-CT scans allow for at least seven pixels to represent the average diameter of the fibers – a resolution that is acceptable for accurate extraction of parameters in 3D that would not be possible with micro-CT or 2D methods such as SEM. This highlights the importance of the use of the methodology represented here in the characterisation of electrospun nano-fibers.
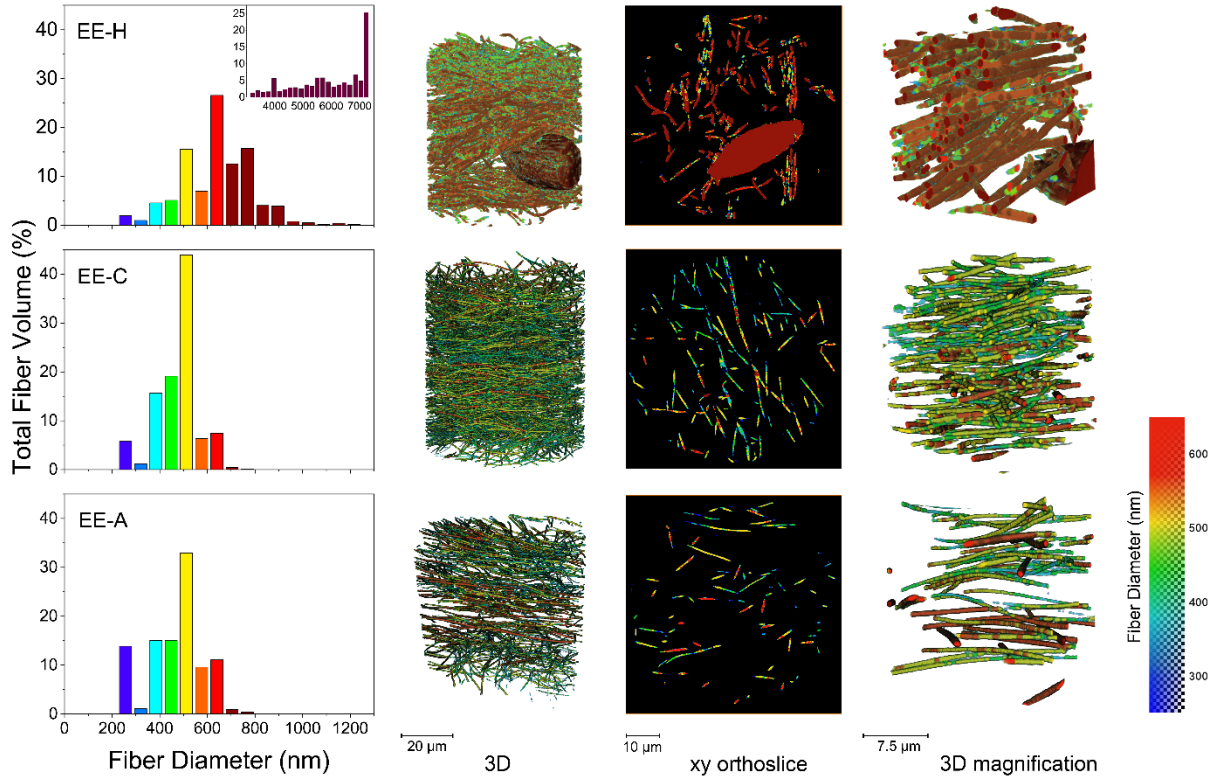
Figure 10: Fiber diameter as calculated using the local thickness method on the whole scan volume of the EE-H (top), EE-C (middle) and EE-A (bottom) electrodes. The histograms of the fiber distributions are shown on the left, with an inset for the EE-H electrode covering the single large fiber. Representations of the local fiber diameter are shown on the right, including the whole volume 3D representation (left), an example *xy* orthoslice (middle) and a magnified area of the 3D visualisation (right). The colour scale is linked to the local fiber diameter, with a progressive opacity applied to the smaller values to avoid them shielding the true colour (diameter) of the fiber at its thickest point. This opacity profile is shown on the colour scale bar.

3.5 Permeability

Table 2 presents the permeability tensor determined for each material. For clarity, the dimensionless permeability is also presented. The dimensionless permeability is defined according to:

$$K_{\mathrm{dim}} = \frac{K}{d_f^2}$$

1

where K is the permeability coefficient [m^2] and d$_f$ is the fiber diameter [m].

Table 2: Compiled permeability coefficients for each sample in each direction. Dimensionless permeability is also presented.

		Permeability	Dimensionless Permeability
		[m²]	[--]
EE-H1	*x*	$1.1E^{-10}$	272.3
	y	$6.03E^{-12}$	14.9
	z	$1.21E^{-10}$	300.0
EE-H2	*x*	$1.34E^{-11}$	33.2
	y	$2.15E^{-11}$	53.2
	z	$1.5E^{-11}$	37.0
EE-C	*x*	$2.65E^{-11}$	116.4
	y	$2.66E^{-11}$	116.8
	z	$2.2E^{-11}$	96.9
EE-A	*x*	$1.01E^{-10}$	460.6
	y	$7.41E^{-11}$	337.1
	z	$5.03E^{-11}$	228.5

A visual representation of this data can be seen in Figure 11 where each component of each materials' permeability tensor is shown as the percentage deviation from the mean permeability in that material. Visualizing the data in this way indicates the shape of the permeability tensor which can is not as easily apparent from simply listing the numbers. The results match the presented theory very well. Due to a significantly larger fiber in the middle of EE-H1, its *y*-component is very small; essentially no flow would be pass through that region in that direction. Conversely the permeability in the other two directions is very high. This anomalously large fiber doesn't just block access to the flow, but also creates regions of very large pores immediately adjacent to it. Features such as these are very detrimental to achieving homogenous flow through the material. In the absence of a large 'outlier' fiber, the other region of this material EE-H2 shows more consistent permeabilities, with much lower deviation. However, there are still considerable inconsistencies in the permeability tensor. The *x*-component appears lower than expected, having even lower permeability than the thru-plane (*z*) direction.

The presence of large heterogeneities and the unpredictable nature of the production of materials of the type presented the previous work [34] and here as EE-H led to the desire for more refined or controlled techniques used to synthesise the EE-C and EE-A materials. EE-C shows a near perfect example of what the permeability tensor should be for isotropic electrospun media. The *x* and *y*-components are nearly identical and significantly higher than the *z*-component. The EE-A material also displays the expected trend, where the highest permeability is the *x*-component, for flow parallel to the majority of fibers, and the lowest component is the z-component, for flow perfectly perpendicular to the fibers. The *y*-component of the permeability tensor has a medial value, representing flow against the alignment of the majority of the fibers but not perfectly perpendicular to them.
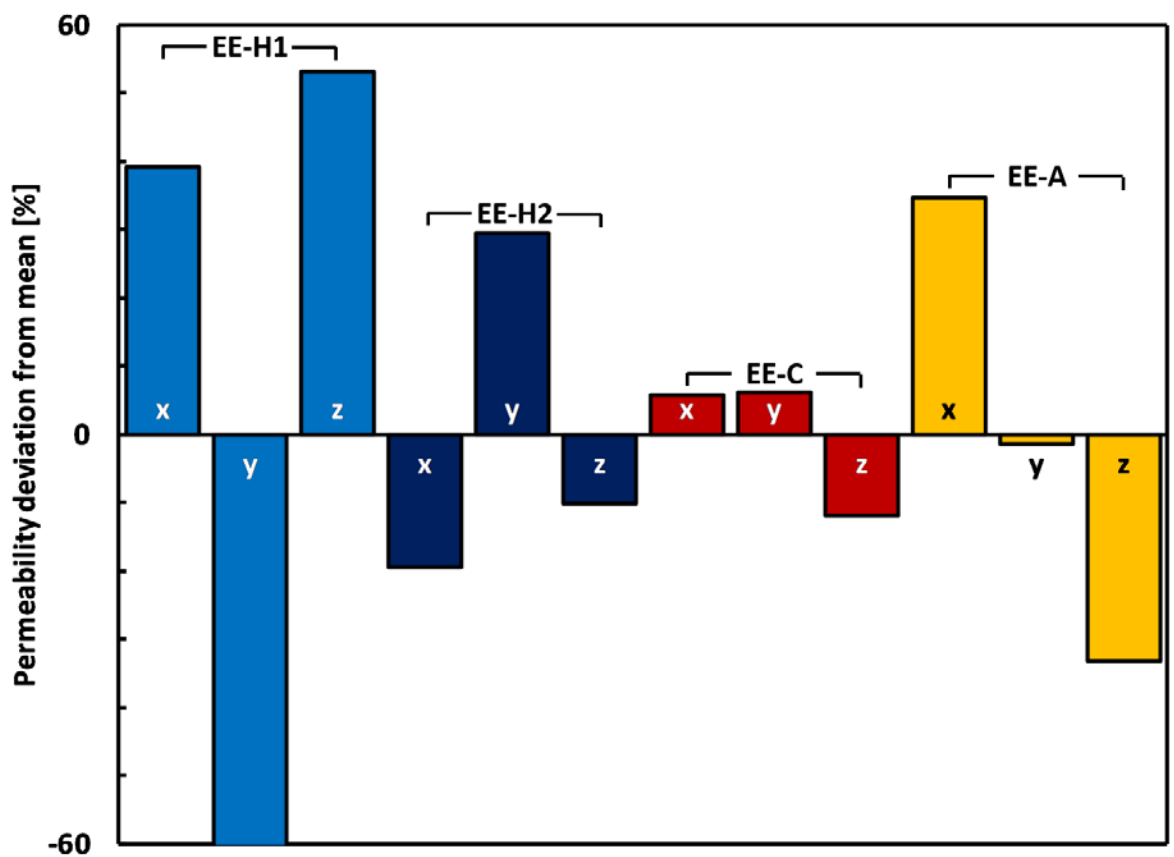

Figure 11: The permeability tensors of all the materials represented as the percentage deviation of each component from that material's mean. The bottom of the y component of EE-H1(light blue) has been trimmed for clarity.

Table 3 Summary of parameters extracted from X-ray CT data. The fiber size for the EE-H sample is given both excluding and including the anomalous single large fiber (*).

Sample	Porosity	Fiber SA/V (μm^{-1})	Tortuosity Factor Pore			Tortuosity Factor Fiber			Average Pore Size (μm)	Average Fiber Diameter (nm)
			x	y	z	x	y	z		
EE-H (total)	82%	3.0								636 (*4,050)
EE-H1	64%	1.4	1.24	1.64	1.36	1.64	10.19	N/A	3.61	
EE-H2	86%	5.4	1.18	1.10	1.21	6.45	2.6	N/A	1.58	
EE-C (total)	93%	7.1								477
EE-C (500^3)	92%	7.0	1.07	1.07	1.11	3.71	2.25	N/A	1.53	
EE-A (total)	96%	7.1								469
EE-A (500^3)	96%	7.8	1.02	1.05	1.06	2.11	8.08	N/A	2.57	

4. Conclusions

For the first time, ultra-high resolution X-ray CT images were obtained of electrospun electrodes with three distinct morphologies. The nano-CT resolution and quality of imaging allowed accurate segmentation of the electrrodes and subsequent computational extraction of parameters. The material without morphological control displayed heterogeneity such as very large fibers and voids that mean the smaller field-of-view of nano-CT is not representative of the whole sample. However, the two materials with controlled fiber morphology and size were consistent throughout the electrode and were therefore suitable for nano-CT imaging. Furthermore, these fibers had an average diameter below 500 nm, meaning that the high resolution of nano-CT was required for sufficient resolution, not achievable with micro-CT employed in previous work. The tortuosity of the materials was simulated and was found to be

directionally dependent for the material with a degree of alignment in the fibers, which could have implications for the design of bespoke electrodes with controlled anisotropy. Additionally, the directional permeability tensors were calculated and showed a similar directional dependence for the aligned material; the highest permeability being in the direction parallel to the alignment of the fibres. This study represents a continuation of previous work into the optimization and characterisation of electrospun materials for use in redox flow batteries, and represents best practice for accurate extraction of parameters from tomographic data of similar electrodes.

5. Acknowledgements

[1.]   Wang, W.; Luo, Q.; Li, B., et al., *Advanced Functional Materials* **2013,** *23* (8), 970-986.
[2.]   Leung, P.; Shah, A. A.; Sanz, L., et al., *Journal of Power Sources* **2017,** *360*, 243-283. DOI http://dx.doi.org/10.1016/j.jpowsour.2017.05.057.
[3.]   Lin, K.; Chen, Q.; Gerhardt, M. R., et al., *Science* **2015,** *349* (6255), 1529-1532. DOI 10.1126/science.aab3033.
[4.]   Chakrabarti, M. H.; Brandon, N. P.; Hajimolana, S. A., et al., *Journal of Power Sources* **2014,** *253*, 150-166. DOI http://dx.doi.org/10.1016/j.jpowsour.2013.12.038.

[5.]   Tjaden, B.; Brett, D. J. L.; Shearing, P. R., *International Materials Reviews* **2016**, 1-21. DOI 10.1080/09506608.2016.1249995.

[6.]   Chen-Wiegart, Y.-c. K.; Shearing, P.; Yuan, Q., et al., *Electrochemistry Communications* **2012,** *21*, 58-61. DOI http://dx.doi.org/10.1016/j.elecom.2012.04.033.

[7.]   Cooper, S. J.; Eastwood, D. S.; Gelb, J., et al., *Journal of Power Sources* **2014,** *247*, 1033-1039. DOI http://dx.doi.org/10.1016/j.jpowsour.2013.04.156.

[8.]   Di Michiel, M.; Merino, J. M.; Fernandez-Carreiras, D., et al., *Review of Scientific Instruments* **2005,** *76* (4), 043702. DOI doi:http://dx.doi.org/10.1063/1.1884194.

[9.]   Finegan, D. P.; Scheel, M.; Robinson, J. B., et al., *Nature communications* **2015,** *6*.

[10.]   Finegan, D. P.; Tudisco, E.; Scheel, M., et al., *Advanced Science* **2016,** *3* (3). DOI 10.1002/advs.201500332.

[11.]   Paz-Garcia, J. M.; Taiwo, O. O.; Tudisco, E., et al., *Journal of Power Sources* **2016,** *320* (Supplement C), 196-203. DOI https://doi.org/10.1016/j.jpowsour.2016.04.076.

[12.]   Nelson, G. J.; Harris, W. M.; Lombardo, J. J., et al., *Electrochemistry Communications* **2011,** *13* (6), 586-589.

[13.]   Shearing, P.; Bradley, R.; Gelb, J., et al., *Solid State Ionics* **2012,** *216*, 69-72.

[14.]   Guan, Y.; Li, W.; Gong, Y., et al., *Journal of Power Sources* **2011,** *196* (4), 1915-1919.

[15.]   Shearing, P.; Bradley, R.; Gelb, J., et al., *Electrochemical and Solid-State Letters* **2011,** *14* (10), B117-B120.

[16.]   Shearing, P.; Gelb, J.; Brandon, N., *Journal of the European Ceramic Society* **2010,** *30* (8), 1809-1814.

[17.]   Shearing, P.; Gelb, J.; Yi, J., et al., *Electrochemistry Communications* **2010,** *12* (8), 1021-1024.

[18.]   Izzo, J. R.; Joshi, A. S.; Grew, K. N., et al., *Journal of The Electrochemical Society* **2008,** *155* (5), B504-B508.

[19.]   Heenan, T. M. M.; Robinson, J.; Lu, X., et al., *Understanding the thermo-mechanical behaviour of solid oxide fuel cell anodes using synchrotron X-ray diffraction.* **2017**.

[20.]   Hack, J.; Heenan, T. M. M.; Iacoviello, F., et al., *Journal of The Electrochemical Society* **2018,** *165* (6), F3045-F3052. DOI 10.1149/2.0051806jes.

[21.]   Hartnig, C.; Manke, I.; Schloesser, J., et al., *Electrochemistry Communications* **2009,** *11* (8), 1559-1562. DOI http://dx.doi.org/10.1016/j.elecom.2009.05.047.

[22.]   Hartnig, C.; Manke, I.; Kuhn, R., et al., *Applied Physics Letters* **2008,** *92* (13), 134106. DOI doi:http://dx.doi.org/10.1063/1.2907485.

[23.]   Manke, I.; Hartnig, C.; Grünerbel, M., et al., *Applied Physics Letters* **2007,** *90* (17), 174105. DOI doi:http://dx.doi.org/10.1063/1.2731440.

[24.]   Meyer, Q.; Mansor, N.; Iacoviello, F., et al., *Electrochimica Acta* **2017,** *242*, 125-136.

[25.]   Meyer, Q.; Ashton, S.; Boillat, P., et al., *Electrochimica Acta* **2016,** *211*, 478-487.

[26.]   Zenyuk, I. V.; Parkinson, D. Y.; Connolly, L. G., et al., *Journal of Power Sources* **2016,** *328*, 364-376. DOI https://doi.org/10.1016/j.jpowsour.2016.08.020.

[27.]   Liu, X.; Jervis, R.; Maher, R. C., et al., *Advanced Materials Technologies* **2016,** *1* (9).

[28.]   Abouelamaiem, D. I.; He, G.; Parkin, I., et al., *Sustainable Energy & Fuels* **2018**. DOI 10.1039/C7SE00519A.

[29.]   Brown, L. D.; Neville, T. P.; Jervis, R., et al., *Journal of Energy Storage* **2016,** *8*, 91-98.

[30.]   Jervis, R.; Brown, L. D.; Neville, T. P., et al., *Journal of Physics D: Applied Physics* **2016,** *49* (43), 434002.

[31.]   Jervis, R.; Brown, L. D.; Neville, T. P., et al., *Journal of Physics D: Applied Physics* **2016,** *49* (43), 434002.

[32.]   Brown, L. D.; Neville, T. P.; Jervis, R., et al., *Journal of Energy Storage* **2016,** *8*, 91-98. DOI http://dx.doi.org/10.1016/j.est.2016.10.003.

[33.] Jervis, R.; Kok, M. D. R.; Neville, T. P., et al., *Journal of Energy Chemistry* **2018**. DOI https://doi.org/10.1016/j.jechem.2018.03.022.

[34.] Kok, M. D. R.; Jervis, R.; Brett, D., et al., *Small* **2018**, 1703616. DOI 10.1002/smll.201703616.

[35.] Meyer, Q.; Mansor, N.; Iacoviello, F., et al., *Electrochimica Acta* **2017**.

[36.] Lu, X.; Li, T.; Taiwo, O. O., et al., *Journal of Physics: Conference Series* **2017,** *849* (1), 012020.

[37.] Taiwo, O. O.; Finegan, D. P.; Gelb, J., et al., *Chemical Engineering Science* **2016**. DOI http://dx.doi.org/10.1016/j.ces.2016.04.023.

[38.] Taiwo, O. O.; Finegan, D. P.; Eastwood, D. S., et al., *Journal of microscopy* **2016,** *263* (3), 280-292. DOI 10.1111/jmi.12389.

[39.] Trogadas, P.; Taiwo, O. O.; Tjaden, B., et al., *Electrochemistry Communications* **2014,** *48* (0), 155-159. DOI http://dx.doi.org/10.1016/j.elecom.2014.09.010.

[40.] Lu, X.; Tjaden, B.; Bertei, A., et al., *Journal of The Electrochemical Society* **2017,** *164* (4), F188-F195. DOI 10.1149/2.0111704jes.

[41.] Tjaden, B.; Lane, J.; Withers, P. J., et al., *Solid State Ionics* **2016,** *288*, 315-321. DOI https://doi.org/10.1016/j.ssi.2016.01.030.

[42.] Haider, A.; Haider, S.; Kang, I.-K., *Arabian Journal of Chemistry* **2015**. DOI https://doi.org/10.1016/j.arabjc.2015.11.015.

[43.] Ma, X.; Kolla, P.; Yang, R., et al., *Electrochimica Acta* **2017,** *236*, 417-423. DOI https://doi.org/10.1016/j.electacta.2017.03.205.

[44.] Freitag, K. M.; Kirchhain, H.; Wüllen, L. v., et al., *Inorganic Chemistry* **2017,** *56* (4), 2100-2107. DOI 10.1021/acs.inorgchem.6b02781.

[45.] Ding, Y.; Hou, H.; Zhao, Y., et al., *Progress in Polymer Science* **2016,** *61*, 67-103. DOI https://doi.org/10.1016/j.progpolymsci.2016.06.006.

[46.] Liu, X.; Naylor Marlow, M.; Cooper, S. J., et al., *Journal of Power Sources* **2018,** *384*, 264-269. DOI https://doi.org/10.1016/j.jpowsour.2018.02.081.

[47.] Tan, Y.; Lin, D.; Liu, C., et al., *Journal of Materials Research* **2017**, 1-11. DOI 10.1557/jmr.2017.373.

[48.] Ma, X.; Kolla, P.; Zhao, Y., et al., *Journal of Power Sources* **2016,** *325*, 541-548. DOI https://doi.org/10.1016/j.jpowsour.2016.06.073.

[49.] Zhang, S.; Li, D.; Kang, J., et al., *Journal of Applied Polymer Science* **2018,** *0* (0), 46443. DOI doi:10.1002/app.46443.

[50.] Chevalier, S.; Lavielle, N.; Hatton, B. D., et al., *Journal of Power Sources* **2017,** *352*, 272-280. DOI https://doi.org/10.1016/j.jpowsour.2017.03.098.

[51.] Liu, S.; Kok, M.; Kim, Y., et al., *Journal of The Electrochemical Society* **2017,** *164* (9), A2038-A2048. DOI 10.1149/2.1301709jes.

[52.] Kok, M. D. R.; Jervis, R.; Shearing, P. R., et al., *ECS Transactions* **2017,** *77* (11), 129-143. DOI 10.1149/07711.0129ecst.

[53.] Kok, M. D. R.; Khalifa, A.; Gostick, J. T., *Journal of The Electrochemical Society* **2016,** *163* (7), A1408-A1419. DOI 10.1149/2.1281607jes.

[54.] Rashapov, R. R.; Unno, J.; Gostick, J. T., *Journal of The Electrochemical Society* **2015,** *162* (6), F603-F612. DOI 10.1149/2.0921506jes.

[55.] Carta, R.; Palmas, S.; Polcaro, A. M., et al., *Journal of Applied Electrochemistry* **1991,** *21* (9), 793-798. DOI 10.1007/bf01402816.

[56.] Tomadakis, M. M.; Robertson, T. J., *Journal of Composite Materials* **2005,** *39* (2), 163-188.

[57.] Gostick, J. T.; Fowler, M. W.; Pritzker, M. D., et al., *Journal of Power Sources* **2006,** *162* (1), 228-238. DOI https://doi.org/10.1016/j.jpowsour.2006.06.096.

[58.]   Zhang, L.; Aboagye, A.; Kelkar, A., et al., *Journal of Materials Science* **2014,** *49* (2), 463-480. DOI 10.1007/s10853-013-7705-y.

[59.]   Kok, M. D. R.; Gostick, J. T., *Journal of Membrane Science* **2015,** *473* (Supplement C), 237-244. DOI https://doi.org/10.1016/j.memsci.2014.09.017.

[60.]   Bailey, J. J.; Heenan, T. M. M.; Finegan, D. P., et al., *Journal of microscopy* **2017,** *267* (3), 384-396. DOI 10.1111/jmi.12577.

[61.]   Tkachuk, A.; Duewer, F.; Cui, H., et al., X-ray computed tomography in Zernike phase contrast mode at 8 keV with 50-nm resolution using Cu rotating anode X-ray source. In *Zeitschrift für Kristallographie - Crystalline Materials*, **2007**; Vol. 222, p 650.

[62.]   Eastwood, D. S.; Bradley, R. S.; Tariq, F., et al., *Nuclear Instruments and Methods in Physics Research Section B: Beam Interactions with Materials and Atoms* **2014,** *324* (Supplement C), 118-123. DOI https://doi.org/10.1016/j.nimb.2013.08.066.

[63.]   Kumar, A. S.; Mandal, P.; Zhang, Y., et al., *Journal of Applied Physics* **2015,** *117* (18), 183102. DOI 10.1063/1.4919835.

[64.]   Cooper, S. J.; Bertei, A.; Shearing, P. R., et al., *SoftwareX* **2016,** *5* (Supplement C), 203-210. DOI https://doi.org/10.1016/j.softx.2016.09.002.

[65.]   Schindelin, J.; Arganda-Carreras, I.; Frise, E., et al., *Nature Methods* **2012,** *9*, 676. DOI 10.1038/nmeth.2019 https://www.nature.com/articles/nmeth.2019#supplementary-information.

[66.]   Münch, B.; Holzer, L., *Journal of the American Ceramic Society* **2008,** *91* (12), 4059-4067. DOI 10.1111/j.1551-2916.2008.02736.x.

[67.]   Januszewski, M.; Kostur, M., *Computer Physics Communications* **2014,** *185* (9), 2350-2368. DOI https://doi.org/10.1016/j.cpc.2014.04.018.

[68.]   Wim Degruyter; A. Burgisser; Bachmann, O., et al., *Geosphere* **2010,** *6* (5), 470-481. DOI 10.1130/GES00555.1.

[69.]   Ismail, M. S.; Damjanovic, T.; Ingham, D. B., et al., *Journal of Power Sources* **2010,** *195* (9), 2700-2708. DOI https://doi.org/10.1016/j.jpowsour.2009.11.069.